Sustainable Energy & Fuels

Interdisciplinary research for the development of sustainable energy technologies

Accepted Manuscript

This article can be cited before page numbers have been issued, to do this please use: J. Kim, J. Hwang, Y. Sun and J. Hassoun, *Sustainable Energy Fuels*, 2019, DOI: 10.1039/C9SE00259F.

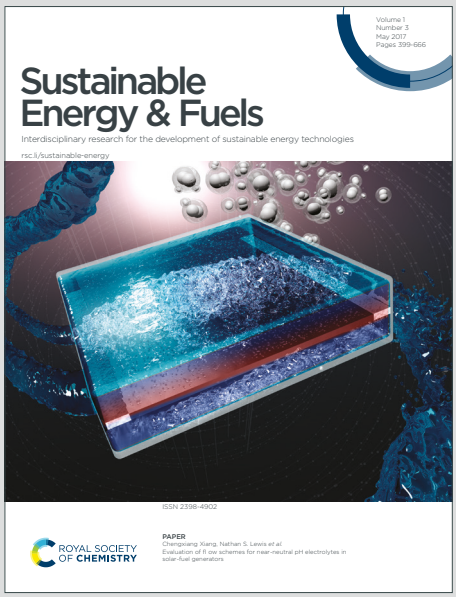

This is an Accepted Manuscript, which has been through the Royal Society of Chemistry peer review process and has been accepted for publication.

Accepted Manuscripts are published online shortly after acceptance, before technical editing, formatting and proof reading. Using this free service, authors can make their results available to the community, in citable form, before we publish the edited article. We will replace this Accepted Manuscript with the edited and formatted Advance Article as soon as it is available.

You can find more information about Accepted Manuscripts in the Information for Authors.

Please note that technical editing may introduce minor changes to the text and/or graphics, which may alter content. The journal's standard Terms & Conditions and the Ethical guidelines still apply. In no event shall the Royal Society of Chemistry be held responsible for any errors or omissions in this Accepted Manuscript or any consequences arising from the use of any information it contains.

View Article Online
DOI: 10.1039/C9SE00259F

A Single Layer of Fe_3O_4@TiO_2 Submicron Spheres as High-Performance Electrode for Lithium-Ion Microbattery

Jung-Min Kim, Jun-Ki Hwang, Yang-Kook Sun, and Jusef Hassoun**

J. M. Kim
Department of Chemical Engineering, College of Engineering, Hanyang University, Seoul 133-791, Republic of Korea
J. K. Hwang, Prof. Y. K. Sun
Department of Energy Engineering, College of Engineering, Hanyang University, Seoul 133-791, Republic of Korea
E-mail: yksun@hanyang.ac.kr
Prof. J. Hassoun
Department of Chemical and Pharmaceutical Sciences, University of Ferrara, Via Fossato di Mortara, 17, 44121, Ferrara, Italy
E-mail: jusef.hassoun@unife.it

Keywords

Single-layer electrode; core-shell Fe_3O_4@TiO_2 spheres; microbattery; lithium ion; high performance

Abstract

High-capacity electrodes with an ultrathin layer configuration represent a suitable component for modern microbatteries. Herein, we report a simple approach consisting of spin-coating and subsequent heat treatment to achieve a single-layer electrode of Fe_3O_4@TiO_2 core-shell submicron spheres. The single-layer electrode operates *via* conversion and insertion reactions with lithium, which is favored by a thin carbon interlayer between the active particles and the copper substrate, without any polymeric binder or nanosized conductive additive. The lithium-ion reaction kinetics and charge transfer characteristics are enhanced by the fine morphological tuning of the electrode particles as well as by the thin carbon interlayer. Indeed, lithium cells using the Fe_3O_4@TiO_2 core-shell submicron spheres and thinnest carbon interlayer exhibit a life that extends over 400 cycles with excellent capacity retention and very high rate capability. These characteristics facilitate the application of the proposed electrode in high-performance Li-ion microbatteries.

View Article Online
DOI: 10.1039/C9SE00259F

1. Introduction

1.1 Lithium-ion microbatteries

The lithium-ion microbattery represents an emerging system that is particularly suitable for miniaturized tools in the electronics[1] and medical fields,[2] as well as for the market in electric vehicles.[3] Hence, a continuously increasing need for high-energy content has triggered research and development efforts aimed at developing new materials characterized by thin-film configurations, high-energy content, suitable stability and reliability, and low cost.[4] The latter factor particularly affects the practical, large-scale diffusion of efficient and high-energy materials for microbatteries.[5] Indeed, a thin film with high performance, in terms of its energy density, cycle life, and suitable scalability to the microbattery level generally requires very complex synthetic pathways characterized by a particularly relevant economic impact.[5,6] Cost-effective microbatteries may be useful in medical applications such as heart pacemakers and artificial body appendixes,[2] while large-scale diffused electronics and electric vehicles require cheap energy storage systems. [5–7] Rechargeable thin-film microbatteries are currently growing in popularity in view of possible applications as wearable energy storage systems[8] and are particularly suitable for advanced medical devices,[9] aerospace systems, miniaturized electronics, and side roles in new generation electric vehicles (EVs) and renewable energy storage systems (ESSs).[1,5,10] Indeed, active materials with a high energy content and minimal size play a key role in promoting the large-scale diffusion of these systems, which can accommodate only miniaturized cell components, i.e., cathode, anode, separator, and electrolyte.[1,5,10] Recent works described

1.2 Cathodes for Li-ion microbatteries

$LiCoO_2$ is the most diffused cathode of rechargeable lithium microbatteries according to various preparation techniques including radio frequency (RF), magnetron sputtering,[11] pulsed laser deposition (PLD),[12,13] chemical vapor deposition,[14] and electroplating.[15] By contrast,

View Article Online
DOI: 10.1039/C9SE00259F

hydrothermal[16] and sol-gel thin film production were attempted[17,18] because ultrahigh energy density can be reached exclusively by using a single-layer electrode and avoiding inactive multiple layers. A thin-film $LiMn_2O_4$ spinel is considered a suitable alternative for microbatteries since it exhibits comparable specific capacity to $LiCoO_2$, can be used at high voltage, and employs the abundant lowly toxic element manganese. $LiMn_2O_4$ thin films have been developed for microbatteries with various thicknesses and porosity degrees by electrostatic spray deposition (ESD),[19] pulsed laser deposition (PLD),[20] radio frequency (RF) magnetron sputtering,[21–23] reactive electron beam evaporation (RBE),[24,25] and sol-gel pathways.[26] Among the cathodes, lithium rich, manganese and nickel substituted lithium cobalt oxides (i.e., $Li_{1+x}Ni_aMn_bCo_cO_2$) represent the most energetic and promising materials for Li-ion battery.[27] An inkjet-printed 3D, Li-rich NMC cathode ($Li_{1.2+x}Mn_{0.54}Ni_{0.13}Co_{0.13}O_2$, $0<x<0.05$) with capacity of about 250 mAh g^{-1} was recently proposed as a suitable material. The separation of the large agglomerates from the cathode by centrifugation has led to active material with a size of less than 140 nm which was considered well meeting the requirements for ink-inkjet of cathode suitable for microbattery application.[28] An olivine-structured $LiFePO_4$ cathode has slightly lower voltage than $LiCoO_2$ and comparable capacity; however, it is characterized by a very long cycle life and rate capability.[29] In addition, this material may be very suitable for thin-layer configurations since its morphology may be finely controlled at the micro- and nanometric levels both in the laboratory[30] and in large-scale production plants.[31] Hence, this material is considered a promising candidate for application in high-performance microbatteries.[29,32]

1.3 Anodes for Li-ion microbatteries

Lithium metal thin films are commonly used as high-capacity anodes in Li microbatteries[33]. However, Li suffers from issues ascribed to dendrite formation and possible internal cell short circuiting.[34] Therefore, the use of high-capacity thin film anodes has considered an effective

View Article Online
DOI: 10.1039/C9SE00259F

approach in achieving efficient Li-ion microbatteries with an enhanced cycle life. This configuration was indicated as particularly favorable for use in miniaturized microbatteries in which the surface nature and configuration play a relevant role in achieving high performance in terms of the energy density and rate capability.[5] Physical vapor deposition (PVD)[36] and chemical vapor deposition (CVD)[37] have been proposed as suitable strategies for preparing thin films with limited concentrations of conductive materials and polymeric binders to increase the energy density. Electrodeposition and pinning were proposed as suitable preparation techniques and alternatives to PVD and CVD, which are affected by limiting factors such as poor film uniformity depending on the characteristic delivery of reactive gases, complexity, relevant cost, and the formation of undesired byproducts.[38] Thin layers and nanostructured materials confined in matrixes of various natures based on lithium-alloying reactions (e.g., silicon,[39–43] tin,[44] and germanium[45]) as well as metal oxides reacting with lithium according to a conversion mechanism (e.g., copper oxide[46] and iron oxides[43,47]) have been studied as alternative high-capacity anodes. The thin film and nanostructured configurations were able to buffer the relevant volume changes during the electrochemical processes of these high-capacity electrodes, which are particularly severe during Li alloying,[48] as well as the high polarization of the Li-conversion reaction.[46]

Despite a capacity limited to 160 mAh g^{-1} and a relatively high working voltage (about 1.5 V), $Li_4Ti_5O_{12}$ (LTO) represents a useful anode material for microbatteries owing to its modest volume expansion during cycling and hence an excellent cycle life.[32,49,50] Therefore, LTO was successfully prepared for this matter by using sol-gel,[51,52] pulsed laser deposition,[53] and magnetron sputtering.[54] Furthermore, microbatteries with complex electrode designs can be prepared by using anode materials such as Ni-Sn alloy and TiO_2, which can be electroplated or sputtered by atomic layer deposition according to topologically complex objects. Accordingly, electrodeposited Ni-Sn anodes have been successfully prepared as high-

View Article Online
DOI: 10.1039/C9SE00259F

performance 3D thin films,[44] while anatase TiO_2 film suitable for use in microbatteries was obtained by using atomic layer deposition.[55]

Single layers of spherical particles have been studied in a variety of fields such as photonic crystals,[56] optical sensors,[57] biosensors,[58] photovoltaics,[59] and light manipulation devices.[60] In this work, we propose a single layer of core-shell-type iron oxide@titanium dioxide (indicated by the acronym Fe_3O_4@TiO_2) submicron spheres having a high energy density as an alternative electrode for lithium-ion microbatteries. The electrode advantageously avoids undesirable supplementary interfaces between the liquid electrolyte and the active material and delivers a high specific capacity and long cycle life in a lithium cell. The TiO_2 shell accommodates the volume expansion of the iron oxide core material, thus allowing for relevant electrochemical, chemical, and thermal stability. Single particles of the electrode are connected via point adhesion to a thin carbon interlayer formed on the surface of the copper foil substrate. This avoids the use of the polymeric binders and conductive material typically employed in electrode preparation. Furthermore, the thin-film electrode exhibits a relatively low irreversible capacity at the first cycle, low polarization, excellent rate capability, and remarkable capacity retention.

Hierarchical Fe_3O_4 hollow spheres with unique structural features, prepared by solvothermal synthesis using Fe–glycerate hollow spheres, exhibited excellent electrochemical lithium storage performance, with capacity ranging from 1200 to 500 mAh g^{-1}, current values from 0.5 A g^{-1} to 10 A g^{-1}, and cycle life extending up 100 cycles.[61] A metal–organic framework (MOF)-assisted strategy was used for the synthesis of a hierarchical hybrid nanostructure composed of Fe_2O_3 nanotubes assembled in Co_3O_4 host. The material revealed excellent electrochemical performance in lithium-ion batteries, with capacity ranging from 700 to 500 mAh g^{-1}, current values from 0.1 A g^{-1} to 2 A g^{-1}, and cycle life extending up 80 cycles (Nano-Micro Letters 2018, 10, 44).[62] A self-assembled flower-like Fe_3O_4/C

View Article Online
DOI: 10.1039/C9SE00259F

architecture was synthesized via two-step method including a solvo-hydrothermal self-assembly process and a high temperature in situ carbonization process.[63] The flower-like Fe_3O_4/C showed a capacity ranging from 1100 to 500 mA h g^{-1} at current from 0.1 to 4.6 A g^{-1}, and cycle life extending to 1000 cycle.[63] Furthermore, anatase nano-TiO_2/carbon hybrid material synthesized by a simple tailored sol–gel pathway was proposed as anode material for lithium battery.[64] The nano-TiO_2–C hybrid material delivered from 170 mA h g^{-1} to 60 mAh g^{-1} at current extending from 0.01 to 5 A g^{-1}, and cycle life up to 1000 cycles.[64] A nanosized rutile TiO_2 prepared by sol–gel technique was also proposed for application in lithium ion battery with a capacity ranging from 200 to 100 mAh g^{-1} and rate capability from 0.07 to 10 A g^{-1}.[65] Several nanostructured conversion-type anode materials with adequate characteristics were reported in a recent review paper.[66] For a suitable comparison with the material studied herein, Table 1 summarizes the performances of Fe_3O_4 and TiO_2 anodes suitable for possible application in Li-ion micro battery.

Table 1

The most relevant point of our work, beside the various iron oxide and titanium oxide-based electrodes reported in literature,[61–66] is represented by the synthesis of a binder free single layer of Fe_3O_4-TiO_2 spheres rather active material powder. The key aspects of this electrode setup with respect to previous works[67] are represented by the high practical capacity due to the absence of polymeric binder, and, at the same time, the particular suitability for miniaturized battery, such as the microbattery, due to the single layer design.

2. Experimental Section

Materials: Methacrylic acid (MAA, purity 99%, Sigma Aldrich) and ethyleneglycoldimethacrylate (EGDMA, TCI) were used without further purification. α,α'-Azobis (isobutyronitrile) (AIBN, Junsei) was recrystallized to remove inhibitors from methanol before use. Ammonium hydroxide (NH_4OH, ~28%, Daejung Chemical), distilled

View Article Online
DOI: 10.1039/C9SE00259F

water, acetonitrile (AN, Daejung Chemical), and ethyl alcohol (anhydrous, 99.9%, Samchun) were used as the solvents. Iron (II) chloride tetrahydrate (Wako), iron (III) chloride anhydrous (Junsei), titanium (Ⅳ) butoxide (Sigma-Aldrich), polymethylsiloxane (PDMS, Sylgard 184, Dow Corning), and polyvinyl alcohol (PVA, Mw = 8.5 × 104 to 12.4 × 104 g mol^{-1}) were used as received. The above abbreviations, i.e., MMA, EGDMA, AIBN, AN, PDMS and PVA will be used in the subsequent paragraphs for describing polymer name and synthesis.

Preparation of monodisperse poly(MAA/EGDMA) microspheres: Crosslinked poly(MAA/EGDMA) microspheres (20 wt. %) were used as sacrificial template and prepared through a distillation-precipitation-polymerization process according to our previous paper.[67] The reaction was performed in a glass reactor without mechanical stirring. MAA (16 g) and EGDMA (4 g) were mixed and polymerized for 90 min at 88 ºC in a medium consisting of AN (136 g), deionized water (24 g), and AIBN (0.4 g). EGDMA and AIBN were used as a crosslinker and an initiator, respectively. After polymerization, the remaining residues were removed and purified by centrifugation several times with ethanol and distilled water. The precipitates were then dried in a vacuum.

Preparation of core-shell-type α-Fe_2O_3@TiO_2 submicron spheres: Poly(MAA/EGDMA) microspheres (1 g) were placed in a four-neck flask with DI water (1000 g) and dispersed in an ultrasonicator for 10 min. The solution was stirred and purged with N_2 gas for 2 h at 200 rpm to evenly disperse the particles and remove oxygen from the reactor. Then, iron (II) chloride tetrahydrate (2.35 g) and iron (Ⅲ) chloride hexahydrate (0.87 g) (3.69:1 mole ratio) were dissolved in DI water (250 g), poured into a flask, and continuously stirred for 24 h. After the products were centrifuged several times with ethanol and DI water at 3600 rpm (to remove the residue), the products were re-dispersed in DI water (1000 g). The solution was then bubbled with N_2 gas for 2 h to remove oxygen from the solution. Subsequently, the ammonium hydroxide solution (5 ml), which was used as a reducing agent, was added under

View Article Online
DOI: 10.1039/C9SE00259F

mechanical stirring at 200 rpm. The products were centrifuged several times with ethanol and DI water at 3600 rpm to remove the residue. The iron oxide precursor/poly(MAA/EGDMA) microspheres were then re-dispersed in ethanol 99.9% (1000 g). Titanium (Ⅳ) butoxide (0.0014 mol) was dissolved in ethanol (250 g) and poured into a reactor containing the iron oxide precursor/poly(MAA/EGDMA) microspheres. A sol-gel reaction was carried out for 1 h, 5 h, or 24 h. After the products were centrifuged several times with ethanol at 3600 rpm (to filter the residue), they were dried in a vacuum. Subsequently, the dry powder was heat treated by raising the temperature to 450 ºC at a rate of 3 ºC min^{-1} and holding at 450 ºC for 4 h under an air flow.

Preparation of single-layer electrode with Fe_3O_4@TiO_2 core-shell submicron spheres: The α-Fe_2O_3@TiO_2 core-shell submicron spheres obtained above were assembled on the PDMS film by hand rubbing, that is, a fine manual forced dispersion of selected powder into the substrate used as the electrode support. The pre-polymer and the crosslinking agent were mixed in a beaker (10:1, w:w). The mixed PDMS polymeric solution (12 g) was poured onto a polystyrene Petri dish and placed in an oven at 50 ºC for 6 h. PVA powders (10 g) were dissolved in DI water with a magnetic stirrer spinning at 900–1000 rpm at 70 ºC. The PVA solution was filtered by a sieve with a mesh size of 30 μm. The as-prepared α-Fe_2O_3@TiO_2 powder was placed on the PDMS film and spread by hand rubbing. A PVA film was coated on the copper foil by a spin-coating method (5000 rpm for 10 s) using a PVA solution (5 wt.%). Air bubbles were removed from the viscous PVA solutions by vacuum pumping. Before the PVA film was completely dried, the single-particle layer on the PDMS substrate was moved to the PVA film via stamping. When the PVA film was completely dried, PDMS was exfoliated from the single-particle layer/PVA/Cu foil. After removal of PDMS from the α-Fe_2O_3@TiO_2/PVA/copper foil, heat treatment was conducted for 4 h at 600 ºC under an argon atmosphere to obtain the final electrode (Fe_3O_4@TiO_2). Circular electrodes were punched for cell application with a geometric surface of 1.54 cm^2. Further details on the

View Article Online
DOI: 10.1039/C9SE00259F

preparation scheme and the characteristics of each synthesis step are reported in the manuscript and the Supplementary Information (SI) section.

Characterization: All products were characterized with optical microscopy (OM, B-51, Olympus), X-ray diffraction (XRD, D/MAX RINT 2000, Rigaku), scanning electron microscopy (SEM, JSM-6300, JEOL), focused-ion beam scanning electron microscopy (FIB-SEM, Hitachi S-4800, Hitachi), transmission electron microscopy (TEM, JEM-2000EX, JEOL), high-resolution transmission electron microscopy (HR-TEM, JEM-2100F, JEOL), high resolution (HR) TEM-based X-ray spectroscopy (EDX) elemental mapping analysis, and X-ray nano-imaging with an accelerator using synchrotron radiation (XNI-7C, Pohang Accelerator Laboratory). The carbon interlayer was analyzed with an elemental analyzer (FLASH EA1112, ThermoFisher Scientific) and characterized by Raman spectroscopy.

Electrochemical properties: Electrochemical characterization was carried out using 2032 coin-type cells. The coin-type cells were assembled in a glove box under an argon atmosphere. Li metal foil (1 mm thick) was used as a counterelectrode, and the commercial electrolyte was composed of a 1-M $LiPF_6$ salt in an ethylene carbonate/diethyl carbonate solution (EC/DEC, 1:1 by volume, provided by Techno Semichem Co. Ltd., Korea). The electrochemical performance was studied in the voltage range between 0.02 and 3 V at various current densities to evaluate the rate capability of the electrode, as well as at a constant current density of 3000 mA g^{-1} for the life-cycle determination. The gravimetric capacity and specific currents of the electrodes were referred to the overall mass including the iron oxide spheres and the carbon interlayer. Before the latter long-term cycling test, the cell was subjected to a formation protocol consisting of various cycles at increasing currents within 0.02 and 3 V, that is, 25 mA g^{-1} (2 cycles), 50 mA g^{-1} (5 cycles), 100 mA g^{-1} (5 cycles), 250 mA g^{-1} (5 cycles), 500 mA g^{-1} (5 cycles), and 1000 mA g^{-1} (5 cycles). Electrochemical impedance spectroscopy (EIS) measurements were performed after the rate capability test by using a Zahner Elektrik IM6 analyzer at frequencies ranging from 5 MHz to 100 kHz with an

View Article Online
DOI: 10.1039/C9SE00259F

amplitude of 50 mV. Lithium half-cells with bare Fe_3O_4,[68] anatase[69] and rutile[70] TiO_2 samples with sub-micrometric or nanometric size characterized in previous works were prepared and studied for comparison. The cells were cycled at C/5 rate (1C = 1007, 170, and 335 mA g^{-1} for Fe_3O_4, anatase and rutile TiO_2, respectively). Voltage limits 0 – 3 V for Fe_3O_4 and 1 – 3 V for TiO_2.

3. Results and discussion

Figure 1 illustrates the scheme adopting the core-shell-type α-Fe_2O_3@TiO_2 submicron sphere synthesis and the polymer-template preparation of the single-layer Fe_3O_4@TiO_2 microelectrode. The synthesis of α-Fe_2O_3@TiO_2 submicron spheres begins by achieving a precursor of iron oxide within microspheres obtained by crosslinking MMA and EGDMA, as reported in the Experimental section. The optical microscopy (OM) images of the sample at each stage of preparation are reported in **Figure S1**, which shows the poly(MAA/EGDMA) microspheres swollen in DI water (Fig. S1a), the sample after the addition of the iron oxide precursors, that is, ferrous ions Fe^{2+} and ferric ions Fe^{3+} (Fig. S1b), and the sample after the addition of NH_4OH (Fig. S1c).

The dissolved positive ions (i.e., Fe^{2+} and Fe^{3+}) diffuse into the poly(MAA/EGDMA) network owing to their electrostatic attraction to the negatively charged polymer chains and cause slight shrinking of the swollen poly(MAA/EGDMA) microspheres (Fig. S1b). The subsequent addition of NH_4OH increases the pH and leads to the formation of iron oxide precursors within the polymer microspheres, which slightly increase in size (Fig. S1c). The TiO_2 shell is coated on the surface of the iron oxide precursor/poly(MAA/EGDMA) microspheres by a sol-gel process using titanium butoxide (see scheme of Fig. 1). It is worth mentioning that carboxylic acid groups in poly(MAA/EGDMA) stabilize the precursor in an aqueous solution and significantly enhance the affinity of the microspheres for the

View Article Online
DOI: 10.1039/C9SE00259F

prehydrolyzed tetrabutyltitanate (i.e., titania oligomers), thus leading to the formation of a TiO_2 shell well coated over the surfaces of the iron oxide/poly(MAA/EGDMA) microspheres.

Figure 1

Figure 2 (a, b) shows the Fourier transform infrared (FT-IR) spectra, while **Figure S2** (SI) shows SEM images of precursors collected from each synthesis step described above. All samples reveal a spherical and uniform morphology, with the particle size slightly increased for the iron oxide precursor (Fig. S2c) compared to the bare poly(MAA/EGDMA) microspheres (Fig. S2a). After coating the TiO_2 shell onto the precursor, the morphology does not change significantly. Furthermore, the FT-IR spectra of the three samples before TiO_2 coating (Fig. 2a) show one broad peak at 3448 cm^{-1} and two sharp peaks at 1473 and 1397 cm^{-1}, corresponding to the typical adsorption of the hydroxyl and methyl groups on MAA molecules, as well as absorption peaks at 1269 and 1171 cm^{-1} corresponding to the adsorption of C–O–C in EGDMA molecules.[67]

In particular, the iron oxide/poly(MAA/EGDMA) microsphere precursor (red line) evidences the characteristic peak corresponding to asymmetric bands at 858–831 cm^{-1} that are most likely attributed to Fe–O–Fe absorption. This is absent for the bare poly(MAA/EGDMA) microspheres (black line), thus suggesting actual iron oxide formation in the polymer matrix. Upon TiO_2 coating, the FT-IR spectra (Fig. 2b) show a broad absorption band at 627 cm^{-1} likely corresponding to the Ti-O-Ti stretching motion,[71] and absorption peaks at 1628 cm^{-1} and 1402 cm^{-1} that suggest a relevant content of water and residual organic groups, respectively, in the sample.[71] Core-shell-type α-Fe_2O_3@TiO_2 submicron spheres and, for comparison, bare α-Fe_2O_3 submicron spheres without TiO_2 coating, are obtained upon heat treatment in air of the above two samples. The single-layer microelectrodes (scheme in Fig. 1) are assembled by polymer template coating of the submicron spheres on copper foil and subsequent heat treatment (annealing) at 600 ºC under an argon atmosphere (see Experimental section).

View Article Online
DOI: 10.1039/C9SE00259F

Figure S3 (SI) shows OM images and digital photographs of PDMS films assembled with bare α-Fe_2O_3 and core-shell-type α-Fe_2O_3@TiO_2 submicron spheres before annealing. The figure reveals that the TiO_2 shell coating has a remarkable effect on the assembly of the particles on PDMS films. Indeed, the bare α-Fe_2O_3 submicron spheres appear heterogeneously dispersed and aggregated on the surface, while the core-shell-type α-Fe_2O_3@TiO_2 submicron spheres are compact and uniformly distributed, most likely owing to the optimal surface characteristics of the particles. After annealing under argon, the electrode surface color changes from red to black owing to carbonization of the PVA interlayer used for electrode preparation and to possible crystal structure modification. In order to investigate the abovementioned carbon interlayer, Raman spectroscopy is performed and reported in **Figure S4** (SI) for Fe_3O_4@TiO_2 core-shell submicron sphere electrodes.

The spectrum reveals two main peaks at around 1350 and 1580 cm^{-1} owing to the D and G bands of carbon, respectively.[72] The G band is associated with the allowed E2g optical modes of the Brillouin zone center of crystalline graphite, while the D band is attributed to disorder-allowed phonon modes that become Raman active as a result of a lack of long-range order in amorphous graphitic materials.[72] The relative intensity ratio of the D and G bands, ID/IG, is known to provide information related to the structural characteristics of carbon. The ID/IG ratio of Fe_3O_4@TiO_2 core-shell submicron spheres after the heat treatment was found to be 0.69, thus indicating that the thin carbon interlayer formed between the single layer of particles and the copper foil substrate is represented by amorphous and crystallized carbonaceous material. The presence of the latter amorphous carbon is also suggested by a D band which shows a full width at half maximum (FWHM) slightly greater than 100 cm^{-1}, and is likely owing to the relatively low temperature adopted for the synthesis.[73]

Fig. 2c shows the X-ray diffraction patterns, and the corresponding Rietveld refinement (computed patterns) of the α-Fe_2O_3@TiO_2 core-shell submicron spheres and of the microelectrode prepared using this material upon heat treatment at 600 ºC**.** The figure, and the

View Article Online
DOI: 10.1039/C9SE00259F

Table 2 summarizing the results of XRD patterns Rietveld refinement, evidence that 61% (w:w) of the pristine α-Fe_2O_3 phase (hematite, ICSD # 88418) is converted into a Fe_3O_4 phase with mixed spinel structure (magnetite, ICSD 85177) by reduction during the heat treatment, while possible reflections of TiO_2 shell coated on the Fe_3O_4 submicron spheres cannot be clearly detected. This is most likely owing to the low relative amount of TiO_2 due the adopted materials ratio during synthesis (see experimental section). Therefore, the final electrode is indicated by Fe_3O_4@TiO_2 since Fe_3O_4 phase is predominant compared to Fe_2O_3. Furthermore, Table 2 evidences the expected raise of the crystallite size from about 50 nm to 100 nm induced by the heat treatment at 600 °C.

Figure 2

Table 2

Figure 3 reveals the morphological features performed by SEM (Fig. 3a–d), HR-TEM (Fig. 3e–h), and STEM (Fig. 3i), as well as the STEM-EDX elemental mapping (Fig. 3j–l) of bare α-Fe_2O_3 submicron spheres and core–shell-type α-Fe_2O_3@TiO_2 submicron spheres synthesized by adopting various sol-gel reaction times for the TiO_2 shell coating. In addition, the figure shows the high-magnification SEM images (Fig. 3n) and cross-sectional image (Fig. 3m) of Fe_3O_4@TiO_2 core-shell submicron spheres coated on copper foil (see Experimental section for details). The bare α-Fe_2O_3 submicron spheres (346 nm) have a rough surface (Fig. 3a), while the surface of the α-Fe_2O_3@TiO_2 submicron spheres becomes progressively smooth and their diameter increases as the sol-gel reaction times increase for coating the TiO_2 shell from 1 h (Fig. 3b) to 5 h (Fig. 3c) and to 24 h (Fig. 3d).

The modification of the particle morphology is further evidenced by the HR-TEM images of the bare α-Fe_2O_3 (Fig. 3e) and the particles subjected to a sol-gel reaction at increasing times (Fig. 3f, g, and h). In particular, the formation of the TiO_2 shell is revealed by the inset in Fig, 3h, which shows a clear fringe separated by 0.22 nm corresponding to the (004) lattice plane of TiO_2.[55] The STEM image of core-shell-type α-Fe_2O_3@TiO_2 submicron spheres (Fig.

View Article Online
DOI: 10.1039/C9SE00259F

3i) and the corresponding elemental mapping (Fig. 3j–l) clearly show that titanium and oxygen are distributed throughout the shells of the particles while iron is located in the submicron sphere core. This suggests a TiO_2 coating over the entire α-Fe_2O_3 submicron sphere. Furthermore, the internal structures of the samples appear quite different when examining HR-TEM images that were randomly selected from an extended group of particles. In this scenario, previous works demonstrated that the core of the particle whit hollow, rattle, and hollow-porous structures are mainly formed by Ostwald ripening during the heat treatment.[74,75] The high-magnification SEM image (Fig. 3n) with an inset of an X-ray image observed from the accelerator using synchrotron radiation and, in particular, the cross-sectional image (Fig. 3m) of the Fe_3O_4@TiO_2 core-shell electrode coated on copper foil, clearly indicate that spherical particles of about 300 nm are placed according to a single layer on a carbon interlayer of about 85 nm that coats the copper substrate. Therefore, the electrode may be considered as a single uniform layer of Fe_3O_4@TiO_2 core-shell submicron spheres without any overlapping. In addition, the inset of SEM image in Fig. 3m, showing a cross-sectional detail of the Fe_3O_4@TiO_2 core-shell particles, evidences partially-hollow core which may be induced by possible shrinking of the material core by annealing at 600 °C under Ar used to obtain the single layer electrode. This morphology is particularly suited for application in microbatteries that may benefit from a top-down or bottom-down 3D microelectrode configuration. This leads to a miniaturized size of the cell and, at the same time, high performance in terms of delivered capacity and rate capability.[5]

Figure 3

We subsequently characterized the material in the lithium cell in order to determine the actual applicability of the core-shell-type Fe_3O_4@TiO_2 submicron-sphere single layer (**Figure 4**). It is worth mentioning that the positive impact of TiO_2 coating on α-Fe_2O_3 nanospheres has been already demonstrated in bulk electrode for lithium-ion battery application which revealed a relevant improvement of the electrochemical performances with respect to bare

View Article Online
DOI: 10.1039/C9SE00259F

iron oxide nanospheres in terms of cycle life and stability.[76] Therefore, we have studied the TiO_2 coated nanoparticles as the most suitable material for forming our monolayer nanospheres substrate for application in Li-ion microbattery, while bare and uncoated materials where only considered to clarify the synthesis and structure of the material, rather than the electrochemical performances. Figure 4a shows the galvanostatic charge/discharge profiles during the 1st, 2nd, and 3rd cycles at low current rates of 25 mA g^{-1} (1st and 2nd) and 50 mA g^{-1} (3rd). The first cycle reveals an initial capacity of about 718 mAh g^{-1}, coulombic efficiency of 72.3%, and a different discharge profile compared to the subsequent cycles owing to the formation of a solid electrolyte interface (SEI) layer on the surface of the active material,[77] as well as to the structural reorganization of the electrode upon the conversion reaction between Fe_3O_4 and Li.[47,78]

During the second and third cycles, the columbic efficiency remarkably increases to values higher than 96% as the SEI layer is consolidated.[79] Further insight on the reaction mechanism of Fe_3O_4@TiO_2 core-shell submicron spheres is provided by the dQ/dV plots reported in Fig. 4b. Interestingly, the figure evidences electrochemical activity with lithium in both Fe_3O_4 and of TiO_2. During the cathodic process, the peaks at ~0.97 V and ~0.81 V may be ascribed to the two steps of the lithiation reactions of Fe_3O_4 [$Fe_3O_4 + 2Li^+ + 2e^- + Li_2(Fe_3O_4)$ and $Li_2(Fe_3O_4) + 6Li \rightarrow 4Li_2O + 3Fe^0$], respectively,[80,81] while the small peak at 1.72 V results from Li^+ insertion into the TiO_2 shell. The anodic process evolves with a double merged peak at ~1.9 V, which is related to the reverse oxidation of Fe^0 to Fe_3O_4, and a minor peak at ~2.3 V owing to the extraction of Li^+ from TiO_2.[76] During subsequent cycles, the peaks shift and their shapes change, particularly compared to the first discharge (cathodic) process. This is attributed to the abovementioned reorganization of the material structure and SEI film formation.[47,77,78]

It is worth mentioning that the cell shows a reduction in the charge/discharge polarization by cycling, and the voltage profiles become centered at an average voltage of about 1.1 V.

View Article Online
DOI: 10.1039/C9SE00259F

The rate capability of the electrode is evaluated by charging the cell at 50 mA g^{-1} and increasing the discharge current from 25 to a value as high as 5000 mA g^{-1} within a voltage ranging from 0.02 to 3.0 V. The cycling response of this test is reported in Fig. 4c, while the voltage profiles are illustrated in **Figure S5** (SI). Significantly, the cell delivers first-charge specific capacities of 519, 493, 496, 495, 491, 476, 440, and 420 at 25, 50, 100, 250, 500, 1000, 2500, and 5000 mA g^{-1}, respectively. This suggests an excellent rate capability of the single layer of Fe_3O_4@TiO_2 core-shell submicron spheres.

Furthermore, the test reveals an increase in the delivered capacity to about 580 mAh g^{-1} as the current is lowered back to 50 mA g^{-1}, which may be associated with an activation process of the material induced by a suitable modification of the structure and enhancement of the SEI in terms of the ion conductivity by cycling, as already observed for other materials.[82] Indeed, continuous cycling may actually lead to a progressive increase in the number of active sites where lithium ions can react, thus enhancing the reversible capacity.[83] The optimal electrode/electrolyte interphase allowing for such a relevant rate capability is further evidenced by an electrochemical impedance spectroscopy test of single-layer electrodes after the test with the lithium cell (Fig. 4d). The corresponding Nyquist plot is studied by a Nonlinear Least Squares (NLLSQ) fitting using a Boukamp tool[84,85] using an equivalent circuit of the type $R_e(R_1Q_1)Q_2$ where, besides the electrolyte resistance R_e, the (R_1Q_1) element represents a medium-to-high-frequency semicircle ascribed to the electrode/electrolyte interphase. This includes the SEI film, charge transfer resistances as the voltage after cell relaxation was below 2V, and constant phase elements (CPE), while the low-frequency element (Q_2) is the tilted line ascribed to the common Warburg diffusion of the lithium ions into the electrode/electrolyte interphase and the geometrical cell capacity.[86] The electrode/electrolyte interphase resistance obtained in **Table S1** (SI) for the electrode used in the cycling with a carbon interlayer 85 nm thick is about 100 Ω, that is, a low value that well justifies the high rate capability.

View Article Online
DOI: 10.1039/C9SE00259F

The cycle life of the single-layer electrode is subsequently evaluated by continuously charging/discharging the cell at a current density as high as 3000 mA g^{-1} (Fig. 4e). In order to avoid a capacity increase during the cycles by the abovementioned activation process, the cell is subjected to a formation protocol prior to testing, as reported in the Experimental section. The cell delivers a very stable capacity over cycles at constant current and reaches a significantly high steady-state value of about 480 mAh g^{-1}. **Figure S6** in SI reports the comparison of lithium half-cells using bare submicron Fe_3O_4 (panel c),[68] anatase (panel a)[69] and rutile (panel b)[70] TiO_2 and Fe_3O_4@TiO_2 submicron spheres (panel d) cycled at C/5 rate (see experimental section for details). The figure clearly shows the improvement promoted by the electrode configuration in the Fe_3O_4@TiO_2 submicron spheres compared to the bare Fe_3O_4 nanoparticles cast onto Cu. Despite the bare Fe_3O_4 reveals higher capacity during the first cycle with respect to Fe_3O_4@TiO_2 submicron spheres, the latter shows remarkably higher stability as ascribed to its optimal configuration. Furthermore, the comparison of the cell performances of Fe_3O_4 samples (Fig. S6 b, c) with TiO_2 samples (Fig. S6 a, b) suggests very limited contribution of the titanium oxide to capacity values and voltage shapes of iron oxide, thus revealing the latter as the most electrochemically relevant part of the electrode and reasonably excluding interactions between TiO_2 and Fe_3O_4 which are supposed to lead to a change in the voltage shape of the active material in lithium cell.

The excellent rate capability and retention, even at very high current, may be attributed to the optimal morphology and structure of the Fe_3O_4@TiO_2 core-shell submicron spheres, as well as to the tin carbon interlayer interposed between the single active layer and the Cu current collector as already evidenced by the cross-sectional SEM image of Fig. 3m. Furthermore, the cross-sectional SEM image of the electrode after long-term cycling (Fig. 4f) reveals a relevant modification of the sample morphology owing to substantial SEI layer formation over the Fe_3O_4@TiO_2 submicron spheres, which remain well attached and adherent to the surface of the copper foil throughout the carbon interlayer. Taking into account a

View Article Online
DOI: 10.1039/C9SE00259F

reversible capacity of about 500 mAh g^{-1}, an average working voltage of about 1.1V vs. Li^+/Li, and possible combination of the studied anode in a full cell with a $LiNi_{0.33}Co_{0.33}Mn_{0.33}O_2$ (NMC) cathode which has a reversible capacity of about 170 mAh g^{-1}, and an average working voltage of about 3.8V vs. Li^+/Li,[87] we can estimate the practical energy density of the Li-ion microbattery using the core-shell-type $Fe_3O_4@TiO_2$ submicron spheres. The above estimation requires a suitable N/P ratio (negative to positive capacity ratio), which is herein supposed of about 1.1.[29] Considering an average mass loading of about 150 μg cm^{-2} of the anode, and the above mentioned N/P ratio and specific capacities, we can calculate for the cathode a mass loading of about 400 μg cm^{-2}. Addition inactive weight contribution, of the same order of the cathode and anode weight, may be considered for electrolyte and current collectors. Therefore, basing on the anode and cathode loadings and their working voltages in half-cell, and taking into account the inactive weight, the above $Fe_3O_4@TiO_2$/NMC full-cell may reach an estimated practical specific capacity of about 80 mAh g^{-1} and average voltage of about 2.7V, thus a practical energy density of about 220 Wh kg^{-1} which is in line with that obtained in new generation Li-ion battery. In is worth mentioning for comparison that graphite generally delivers a capacity approaching 350 mAh g^{-1} at about 0.3 V vs. Li^+/Li, while the electrode studied herein delivers a capacity approaching 600 mAh g^{-1} at 1.1V. These data suggest that possible negative effect of the higher anode discharge voltage of $Fe_3O_4@TiO_2$ with respect to graphite in full cell may be mitigated by the benefit of the higher specific capacity. Furthermore, various bonuses such as missing lithium plating and electrode delamination represent additional safety advantages of the material proposed herein for Li-ion microbattery.

Figure 4

In order to evaluate the effect of the carbon interlayer between Cu and the $Fe_3O_4@TiO_2$ core-shell submicron spheres on the rate capability of the electrode, we performed cycling tests by gradually increasing the thickness. This procedure was particularly adopted to detect

View Article Online
DOI: 10.1039/C9SE00259F

the optimal carbon interlayer thickness suitable for achieving high electrode performance in Li-ion microbattery. **Figure 5** shows cross-sectional SEM images of three electrodes with carbon interlayer thicknesses of (a) 186 nm, (b) 235 nm, and (c) 382 nm, and the corresponding Nyquist plots of the EIS (d, e, and f, respectively) after a cycling test at various currents in a lithium cell and relaxation to a voltage below 2V (**Figure S7** in SI). The corresponding data analysis (Table S1) clearly reveals an almost linear increase in the electrode/electrolyte interphase resistance (see plot of Fig. S7b) from 104 Ω to 822 Ω as the carbon interlayer thickness increases from 85 nm (EIS in Fig. 4d) to 382 nm (EIS in Fig. 5f).

Despite a still-sufficient cycling performance (Fig. S7a), the increase in resistance by increasing the thickness unavoidably lowers the rate capability of the electrode. This is most likely owing to a hindered charge transfer process and slowed kinetics at the electrode electrolyte interphase.[88] Furthermore, the decrease of the low-frequency tilted-line slope in the Nyquist plots of electrodes with increased carbon interlayer thicknesses (Fig. 5d–f) compared to that with a carbon interlayer of 85 nm (Fig. 4d) indicates a hindered Li^+-ion diffusion.[89] Therefore, we may reasonably suppose that the both Li^+-ion diffusion and charge transfer depend greatly on the thickness of the carbon interlayer in the single-layer electrode studied herein. It is worth mentioning that the synthetic pathway adopted in this work may be suitable for changing the size of the spheres from submicron to micron size, thus leading to the control of single layer electrode thickness, still holding its electrochemical performances. Figure S8 in Supplementary Information reports an example in which the size of the active material spheres in the microelectrode has been increased from 0.4 μm (panel a) to 4 μm (panel b), thus leading to the increase of the electrode thickness by a factor of 10.

Figure 5

4. Conclusion

View Article Online
DOI: 10.1039/C9SE00259F

We proposed a novel high-performance single-layer electrode for Li-ion microbattery applications. Core-shell-type α-Fe_2O_3@TiO_2 submicron spheres were synthesized and successfully ordered by using spin-coating and subsequent annealing as a single active layer of Fe_3O_4@TiO_2, which was attached to the current collector through a nanometric carbon interlayer without polymeric binders or conductive additives. The single-layer electrode revealed an enhanced structure and morphology in which the absence of significant particles overlapping was observed. The electrode operated according to a voltage profile centered at about 1.1 V, which reflected the electrochemical processes of both the TiO_2 shell (Li-insertion reaction) and Fe_3O_4 core (Li-conversion reaction). The material exhibited excellent rate capability and a prolonged cycle life in lithium cell, with specific capacity ranging from about 580 mAh g^{-1} at low current values to about 420 mAh g^{-1} at very high currents (i.e., 5 A g^{-1}).

The extremely ordered submicron sphere layer was characterized by changing the thickness of the carbon interlayer connecting it to the Cu support. The data indicated that an increase in the interlayer thickness hinders the electrode performance in terms of capacity and rate capability owing to the linear increase in the charge transfer resistances as well as the limitation of lithium-ion diffusion kinetics at the electrode/electrolyte interphase. Advantageously, this aspect favors the employment of the electrode in its thinnest configuration in a microbattery. Considering a capacity of about 500 mAh g^{-1}, average working voltage (1.1 V), average electrode thickness (about 500 nm), and mass loading of the active material ranging from 150 to 200 μg cm^{-2}, we may estimate for our single-layer core-shell Fe_3O_4@TiO_2 submicron spheres a volumetric energy density exceeding 1500 Wh/L. This value based on anode material only, may be possibly benchmarked into a more practical value such as the one ascribed to the Fe_3O_4@TiO_2 /$LiNi_{0.33}Co_{0.33}Mn_{0.33}O_2$ (NMC) discussed in the work (Fig. 4).[29,87] Therefore, taking into account a thickness of about 20 μm for thin-film microbattery[3] comprising active and inactive components, a working voltage value of

View Article Online
DOI: 10.1039/C9SE00259F

about 2.7V, the above discussed masses loading and capacities (see discussion of Fig. 4 for further details), the Li-ion cell based on submicron spheres may have an estimated practical volumetric energy density of about 150 Wh/L, which fully matches the high-performance requirements of the microbattery.[3] Literature papers reported examples of top-down and bottom-up single layered electrodes for achieving the performance 3D rechargeable lithium microbatteries.[5] Accordingly, micro-battery was fabricated by BAB block copolymer electrolyte and a sol–gel method combined with micro-injection system, using $LiMn_2O_4$ cathode and $Li_4Ti_5O_{12}$ anode.[90] The microbattery with single layer configuration operated at 2.45 V with a discharge capacity of 245 nA h which corresponded to the energy density of 8.48 μWh cm^{-2}. Another Li-ion microbattery was fabricated by coupling 68 μm thick $LiCoO_2$ cathode and carbon anode in PVdF-HFP gel polymer electrolyte (GPE). The battery achieved a maximum power density of 38 mW cm^{-2}.[7] Taking into account the Fe_3O_4@TiO_2 capacity of 500 mAh g^{-1}, and a loading of 150 μg cm^{-2}, the Fe_3O_4@TiO_2/NMC microbattery discussed in Figure 4 has a surface capacity of 75 μAh cm^{-2} and a voltage of 2.7V, which lead to theoretical energy density higher than 200 μWh cm^{-2} for the battery and may be actually reflected into a practical capacity higher than 50 μWh cm^{-2}. Furthermore, a significant applications of the binder free electrode may be the investigation of the lithium oxygen ($Li-O_2$) reaction mechanism, such as the electrochemical impedance spectroscopy (EIS) study reported in literature to provide additional insight on the electrochemical kinetics of the cell.[91]

Acknowledgements

This work was supported by National Research Foundation of Korea (NRF) grant funded by the Korea government Ministry of Education and Science Technology (MEST) (NRF-2018R1A2B3008794) and supported by a Human Resources Development program (no. 20154010200840) of a Korea Institute of Energy Technology Evaluation and Planning

View Article Online
DOI: 10.1039/C9SE00259F

(KETEP) by the Ministry of Trade, Industry and Energy of the Korean government. J.H. thanks the grant "Fondo di Ateneo per la Ricerca Locale (FAR) 2018", University of Ferrara.

References

1 A. Patil, V. Patil, D. Wook Shin, J.-W. Choi, D.-S. Paik and S.-J. Yoon, *Mater. Res. Bull.*, 2008, **43**, 1913–1942.

2 D. C. Bock, A. C. Marschilok, K. J. Takeuchi and E. S. Takeuchi, *Electrochim. Acta*, 2012, **84**, 155–164.

3 Y. Wang, B. Liu, Q. Li, S. Cartmell, S. Ferrara, Z. D. Deng and J. Xiao, *J. Power Sources*, 2015, **286**, 330–345.

4 M. Hallot, A. Demortière, P. Roussel and C. Lethien, *Energy Storage Mater.*, 2018, **15**, 396–406.

5 S. Ferrari, M. Loveridge, S. D. Beattie, M. Jahn, R. J. Dashwood and R. Bhagat, *J. Power Sources*, 2015, **286**, 25–46.

6 A. Piqué, C. B. Arnold, H. Kim, M. Ollinger and T. E. Sutto, *Appl. Phys. A*, 2004, **79**, 783–786.

7 H. Kim, R. C. Y. Auyeung and A. Piqué, *J. Power Sources*, 2007, **165**, 413–419.

8 L. Liu, S. Ryu, M. R. Tomasik, E. Stolyarova, N. Jung, M. S. Hybertsen, M. L. Steigerwald, L. E. Brus and G. W. Flynn, *Nano Lett.*, 2008, **8**, 1965–1970.

9 C. L. Schmidt and P. M. Skarstad, *J. Power Sources*, 2001, **97–98**, 742–746.

10 C. Yue, J. Li and L. Lin, *Front. Mech. Eng.*, 2017, **12**, 459–476.

11 B. Wang, *J. Electrochem. Soc.*, 1996, **143**, 3203.

12 K. A. Striebel, *J. Electrochem. Soc.*, 1996, **143**, 1821.

13 S. Ohta, T. Kobayashi, J. Seki and T. Asaoka, *J. Power Sources*, 2012, **202**, 332–335.

14 J. F. M. Oudenhoven, T. van Dongen, R. A. H. Niessen, M. H. J. M. de Croon and P. H. L. Notten, *J. Electrochem. Soc.*, 2009, **156**, D169.

15 K.-S. Han, S.-W. Song, H. Fujita, M. Yoshimura, E. J. Cairns and S.-H. Chang, *J. Am. Ceram. Soc.*, 2002, **85**, 2444–2448.

16 S.-W. Song, K.-S. Han and M. Yoshimura, *J. Am. Ceram. Soc.*, 2004, **83**, 2839–2844.

17 Y. H. Rho, K. Kanamura and T. Umegaki, *J. Electrochem. Soc.*, 2003, **150**, A107.

18 H. Kim, *J. Laser Micro/Nanoengineering*, 2012, **7**, 320–325.

19 M. Nishizawa, T. Uchiyama, K. Dokko, K. Yamada, T. Matsue and I. Uchida, *Bull. Chem. Soc. Jpn.*, 1998, **71**, 2011–2015.

20 C. Julien, E. Haro-Poniatowski, M. . Camacho-Lopez, L. Escobar-Alarcon and J. Jimenez-Jarquin, *Mater. Sci. Eng. B*, 2000, **72**, 36–46.

21 B.-J. Hwang, C.-Y. Wang, M.-Y. Cheng and R. Santhanam, *J. Phys. Chem. C*, 2009, **113**, 11373–11380.

22 K.-L. Lee, J.-Y. Jung, S.-W. Lee, H.-S. Moon and J.-W. Park, *J. Power Sources*, 2004, **130**, 241–246.

23 Y.-S. Park, *Electrochem. Solid-State Lett.*, 1999, **2**, 58.

24 F. K. Shokoohi, *J. Electrochem. Soc.*, 1992, **139**, 1845.

25 F. K. Shokoohi, J. M. Tarascon and B. J. Wilkens, *Appl. Phys. Lett.*, 1991, **59**, 1260–1262.

26 Y. . Park, J. . Kim, M. . Kim, H. . Chung, W. . Um, M. . Kim and H. . Kim, *J. Power Sources*, 1998, **76**, 41–47.

27 G. A. Elia, J. Wang, D. Bresser, J. Li, B. Scrosati, S. Passerini and J. Hassoun, *ACS Appl. Mater. Interfaces*, 2014, **6**.

28 M. Maximov, D. Kolchanov, Il. Mitrofanov, A. Vinogradov, Y. Koshtyal, A. Rymyantsev and A. Popovich, *Proceedings*, 2018, **3**, 7.

29 D. Di Lecce, R. Verrelli and J. Hassoun, *Green Chem.*, 2017, **19**.

30 S. W. Oh, S.-T. Myung, S.-M. Oh, K. H. Oh, K. Amine, B. Scrosati and Y.-K. Sun, *Adv. Mater.*, 2010, **22**, 4842–4845.

31 S. Brutti, J. Hassoun, B. Scrosati, C.-Y. Lin, H. Wu and H.-W. Hsieh, *J. Power Sources*, 2012, **217**.

32 K. Sun, T.-S. Wei, B. Y. Ahn, J. Y. Seo, S. J. Dillon and J. A. Lewis, *Adv. Mater.*, 2013, **25**, 4539–4543.

33 W. Xu, J. Wang, F. Ding, X. Chen, E. Nasybulin, Y. Zhang and J.-G. Zhang, *Energy Environ. Sci.*, 2014, **7**, 513–537.

34 L. Lu, X. Han, J. Li, J. Hua and M. Ouyang, *J. Power Sources*, 2013, **226**, 272–288.

35 J. Bates, *Solid State Ionics*, 2000, **135**, 33–45.

36 X. Chen, K. Gerasopoulos, J. Guo, A. Brown, C. Wang, R. Ghodssi and J. N. Culver, *ACS Nano*, 2010, **4**, 5366–5372.

37 L.-F. Cui, Y. Yang, C.-M. Hsu and Y. Cui, *Nano Lett.*, 2009, **9**, 3370–3374.

38 X. Meng, X.-Q. Yang and X. Sun, *Adv. Mater.*, 2012, **24**, 3589–3615.

39 J. P. Maranchi, A. F. Hepp and P. N. Kumta, *Electrochem. Solid-State Lett.*, 2003, **6**, A198.

40 C. K. Chan, H. Peng, G. Liu, K. McIlwrath, X. F. Zhang, R. A. Huggins and Y. Cui, *Nat. Nanotechnol.*, 2008, **3**, 31–35.

41 J. R. Szczech and S. Jin, *Energy Environ. Sci.*, 2011, **4**, 56–72.

42 A. Magasinski, P. Dixon, B. Hertzberg, A. Kvit, J. Ayala and G. Yushin, *Nat. Mater.*, 2010, **9**, 353–358.

43 C. Liang, M. Gao, H. Pan, Y. Liu and M. Yan, *J. Alloys Compd.*, 2013, **575**, 246–256.

44 J. Hassoun, S. Panero, P. Simon, P. L. Taberna and B. Scrosati, *Adv. Mater.*, 2007, **19**.

45 S. Goriparti, E. Miele, F. De Angelis, E. Di Fabrizio, R. Proietti Zaccaria and C. Capiglia, *J. Power Sources*, 2014, **257**, 421–443.

46 R. Verrelli, J. Hassoun, A. Farkas, T. Jacob and B. Scrosati, *J. Mater. Chem. A*, 2013, **1**.

47 R. Verrelli, R. Brescia, A. Scarpellini, L. Manna, B. Scrosati and J. Hassoun, *RSC Adv.*, 2014, **4**, 61855–61862.

View Article Online
DOI: 10.1039/C9SE00259F

48 R. Verrelli and J. Hassoun, *J. Power Sources*, 2015, **299**, 611–616.

49 T. Ohzuku, *J. Electrochem. Soc.*, 1995, **142**, 1431.

50 H. G. Jung, M. W. Jang, J. Hassoun, Y. K. Sun and B. Scrosati, *Nat. Commun.*, 2011, **2**.

51 Y. Hao, Q. Lai, D. Liu, Z. Xu and X. Ji, *Mater. Chem. Phys.*, 2005, **94**, 382–387.

52 C. Shen, X. Zhang, Y. Zhou and H. Li, *Mater. Chem. Phys.*, 2003, **78**, 437–441.

53 J. Deng, Z. Lu, I. Belharouak, K. Amine and C. Y. Chung, *J. Power Sources*, 2009, **193**, 816–821.

54 C.-L. Wang, Y. C. Liao, F. C. Hsu, N. H. Tai and M. K. Wu, *J. Electrochem. Soc.*, 2005, **152**, A653.

55 W. Wang, M. Tian, A. Abdulagatov, S. M. George, Y.-C. Lee and R. Yang, *Nano Lett.*, 2012, **12**, 655–660.

56 M. Kolle, P. M. Salgard-Cunha, M. R. J. Scherer, F. Huang, P. Vukusic, S. Mahajan, J. J. Baumberg and U. Steiner, *Nat. Nanotechnol.*, 2010, **5**, 511–515.

57 J.-T. Zhang, L. Wang, J. Luo, A. Tikhonov, N. Kornienko and S. A. Asher, *J. Am. Chem. Soc.*, 2011, **133**, 9152–9155.

58 L. Y. Wu, B. M. Ross and L. P. Lee, *Nano Lett.*, 2009, **9**, 1956–1961.

59 Y. Fang, N.-H. Seong and D. D. Dlott, *Science (80-.).*, 2008, **321**, 388–392.

60 Y.-J. Oh, S.-G. Park, M.-H. Kang, J.-H. Choi, Y. Nam and K.-H. Jeong, *Small*, 2011, **7**, 184–188.

61 F.-X. Ma, H. Hu, H. Bin Wu, C.-Y. Xu, Z. Xu, L. Zhen and X. W. David Lou, *Adv. Mater.*, 2015, **27**, 4097–4101.

62 S. L. Zhang, B. Y. Guan, H. Bin Wu and X. W. D. Lou, *Nano-Micro Lett.*, 2018, **10**, 44.

63 L. Wan, D. Yan, X. Xu, J. Li, T. Lu, Y. Gao, Y. Yao and L. Pan, *J. Mater. Chem. A*, 2018, **6**, 24940–24948.

64 E. Lim, H. Shim, S. Fleischmann and V. Presser, *J. Mater. Chem. A*, 2018, **6**, 9480–9488.

65 P. Kubiak, M. Pfanzelt, J. Geserick, U. Hörmann, N. Hüsing, U. Kaiser and M. Wohlfahrt-Mehrens, *J. Power Sources*, 2009, **194**, 1099–1104.

66 Y. Lu, L. Yu and X. W. (David) Lou, *Chem*, 2018, **4**, 972–996.

67 S.-J. Park, H.-S. Lim, Y. M. Lee and K.-D. Suh, *RSC Adv.*, 2015, **5**, 10081–10088.

68 F. Jiao, J.-C. Jumas, M. Womes, A. V. Chadwick, A. Harrison and P. G. Bruce, *J. Am. Chem. Soc.*, 2006, **128**, 12905–12909.

69 R. Bernhard, A. Latini, S. Panero, B. Scrosati and J. Hassoun, *J. Power Sources*, 2013, **226**, 329–333.

70 J. Hassoun, M. Pfanzelt, P. Kubiak, M. Wohlfahrt-Mehrens and B. Scrosati, *J. Power Sources*, 2012, **217**.

71 M.-Y. G. MAO-PING ZHENG, YAN-PING JIN, GUO-LIANG JIN, *J. Mater. Sci. Lett.*, 2000, **19**, 433 – 436.

72 J. Kastner, T. Pichler, H. Kuzmany, S. Curran, W. Blau, D. N. Weldon, M. Delamesiere, S. Draper and H. Zandbergen, *Chem. Phys. Lett.*, 1994, **221**, 53–58.

73 M. Morel, E. Mosquera, D. E. Diaz-Droguett, N. Carvajal, M. Roble, V. Rojas and R. Espinoza-González, *Int. J. Hydrogen Energy*, 2015, **40**, 15540–15548.

74 J. S. Cho, J.-S. Park and Y. C. Kang, *Sci. Rep.*, 2016, **6**, 38933.

75 H.-S. Lim, Y.-K. Sun and K.-D. Suh, *J. Mater. Chem. A*, 2013, **1**, 10107.

76 Y. Fu, Q. Wei, X. Wang, H. Shu, X. Yang and S. Sun, *J. Mater. Chem. A*, 2015, **3**, 13807–13818.

77 C. He, S. Wu, N. Zhao, C. Shi, E. Liu and J. Li, *ACS Nano*, 2013, **7**, 4459–4469.

78 J. Hassoun, F. Croce, I. Hong and B. Scrosati, *Electrochem. commun.*, 2011, **13**.

79 E. Kang, Y. S. Jung, A. S. Cavanagh, G.-H. Kim, S. M. George, A. C. Dillon, J. K. Kim and J. Lee, *Adv. Funct. Mater.*, 2011, **21**, 2430–2438.

80 J. Luo, J. Liu, Z. Zeng, C. F. Ng, L. Ma, H. Zhang, J. Lin, Z. Shen and H. J. Fan, *Nano Lett.*, 2013, **13**, 6136–6143.

81 R. Ma, L. He, Z. Lu, S. Yang, L. Xi and J. C. Y. Chung, *CrystEngComm*, 2012, **14**, 7882.

82 Y. Ma, U. Ulissi, D. Bresser, Y. Ma, Y. Ji and S. Passerini, *Electrochim. Acta*, 2017, **258**, 535–543.

83 L. Qie, W.-M. Chen, Z.-H. Wang, Q.-G. Shao, X. Li, L.-X. Yuan, X.-L. Hu, W.-X. Zhang and Y.-H. Huang, *Adv. Mater.*, 2012, **24**, 2047–2050.

84 B. A. Boukamp, *Solid State Ionics*, 1986, **18**–**19**, 136–140.

85 B. Boukamp, *Solid State Ionics*, 1986, **20**, 31–44.

86 D. Aurbach, *J. Power Sources*, 2000, **89**, 206–218.

87 D. Di Lecce, P. Andreotti, M. Boni, G. Gasparro, G. Rizzati, J.-Y. Hwang, Y.-K. Sun and J. Hassoun, *ACS Sustain. Chem. Eng.*, 2018, **6**, 3225–3232.

88 D. Lin, Z. Lu, P.-C. Hsu, H. R. Lee, N. Liu, J. Zhao, H. Wang, C. Liu and Y. Cui, *Energy Environ. Sci.*, 2015, **8**, 2371–2376.

89 B.-L. He, B. Dong and H.-L. Li, *Electrochem. commun.*, 2007, **9**, 425–430.

90 H. Nakano, K. Dokko, J. Sugaya, T. Yasukawa, T. Matsue and K. Kanamura, *Electrochem. commun.*, 2007, **9**, 2013–2017.

91 R. Nelson, M. H. Weatherspoon, J. Gomez, E. E. Kalu and J. P. Zheng, *Electrochem. commun.*, 2013, **34**, 77–80.

View Article Online
DOI: 10.1039/C9SE00259F

List of tables

Table 1. Summary of the performances of recently proposed Fe_3O_4 and TiO_2 anodes potentially suitable for Li-ion microbattery.

Table 2. Results of the Rietveld refinement performed on the X-ray diffraction patterns of core-shell-type α-Fe_2O_3@TiO_2 spheres and of sample after heat treatment at 600 ºC in Ar atmosphere adopted for electrode preparation (see corresponding patterns in Fig. 3c).

List of figures

Figure 1. (a) Schematic representation of preparation processes for core-shell-type α-Fe_2O_3@TiO_2 submicron spheres (top side), and single-layer electrode assembled with Fe_3O_4@TiO_2 submicron spheres (bottom side).

Figure 2. **(a)** FT-IR spectra of crosslinked poly(MAA/EGDMA) microspheres (black line), sample after introducing iron oxide precursors (blue line), and sample after subsequent addition of NH_4OH (red line). **(b)** FT-IR spectra of iron oxide precursor/poly(MAA/EGDMA) microspheres with (black) and (red) without TiO_2 shell formed by sol-gel reaction. **(c)** X-ray diffraction patterns, and corresponding Rietveld refinement computed patterns, of core-shell-type α-Fe_2O_3@TiO_2 spheres (grey and black patterns) and of sample after heat treatment at 600 ºC in Ar atmosphere (red and orange patterns) adopted for electrode preparation.

Figure 3. (a–h) SEM and TEM images of **(a, e)** bare α-Fe_2O_3 submicron spheres and core-shell-type α-Fe_2O_3@TiO_2 submicron spheres with different sol-gel reaction times for coating TiO_2 shell, that is, **(b, f)** 1 h, **(c, g)** 5 h, and **(d, h)** 24 h. **(i)** STEM and **(j–l)** STEM-based EDX mapping images of core-shell-type α-Fe_2O_3@TiO_2 submicron spheres with sol-gel reaction time of 24 h after heat treatment at 600 ºC in argon atmosphere: **(j)** Fe, **(k)** O, and **(l)** Ti. **(n)** High-magnification SEM images (inset of X-ray image observed from accelerator using synchrotron radiation) and **(m)** cross-sectional image of Fe_3O_4@TiO_2 core-shell submicron sphere monolayer coated on copper foil, and inset containing a detailed image revealing the partially hollow core of the particles (see experimental section and SI for further details).

View Article Online
DOI: 10.1039/C9SE00259F

Figure 4. **(a)** Voltage profiles and **(b)** differential capacity plots (dQ/dV) of single-layer electrode with Fe_3O_4@TiO_2 core-shell submicron spheres galvanostatically cycled in lithium cell in voltage window between 0.02 and 3 V at 25 mA g^{-1} (1st cycle and 2nd cycle) and 50 mA g^{-1} (3rd cycle). **(c)** Cycling profiles of single-layer electrode at currents ranging from 50 to 5000 mA g^{-1}. **(d)** Nyquist plot of electrochemical impedance spectroscopy of single-layer electrode in lithium cell after rate capability test at frequencies ranging from 5 MHz to 100 kHz with amplitude of 50 mV. **(e)** Long-term cycling test of single-layer electrode in lithium cell at current rate of 2500 mA g^{-1}, and **(f)** cross-sectional SEM image of electrode after test. Electrolyte: EC/DEC (1:1 v/v), $LiPF_6$ 1 M.

Figure 5. Cross-sectional images of single electrodes with increasing average thicknesses of carbon interlayer between Fe_3O_4@TiO_2 core-shell submicron spheres and Cu current collector: **(a)** 186 nm, **(b)** 235 nm, and **(c)** 382 nm. Nyquist plots of electrochemical impedance spectroscopy of above electrodes in lithium cell: **(d)** 186 nm, **(e)** 235 nm, and **(f)** 382 nm. Electrolyte: EC/DEC (1:1 v/v), $LiPF_6$ 1 M. Frequency range 5–100 kHz, signal amplitude of 50 mV.

View Article Online
DOI: 10.1039/C9SE00259F

Material	Synthesis pathway	Capacity range (mAh g^{-1})	Current Range (A g^{-1})	Reported cycles (Cycle number)	Reference
Hierarchical Fe_3O_4 hollow spheres	Solvothermal synthesis	1200 – 500	0.5 – 10	100	61
Hierarchical hybrid nanostructure-Fe_2O_3-Co_3O_4 host	Metal–organic framework (MOF)-assisted strategy	700 – 500	0.1 – 2	80	62
Self-assembled flower-like Fe_3O_4/C	Solvo-hydrothermal self-assembly process	1100 – 500	0.1 – 4.6	1000	63
Anatase nano-TiO_2/carbon hybrid material	Tailored sol–gel pathway	170 – 60	0.01 – 5	1000	64
Nanosized rutile TiO_2	Sol–gel technique	200 – 100	0.07 – 10	80	65

Table 1

View Article Online
DOI: 10.1039/C9SE00259F

Sample	Phase	ICSD	Space group	Symmetry	a (A°)	b (A°)	c (A°)	Crystallite size (nm)
Before heating @ 600 °C	Fe_2O_3 (Hematite)	88418	R-3c:H	Trigonal	5.0376935	-	13.7714	53
After heating @ 600 °C	61% (w:w) Fe_3O_4 (Magnetite)	85177	Fd-3m:2	Cubic	8.40146	-	-	99
	39% (w:w) Fe_2O_3 (Hematite)	88418	R-3c:H	Trigonal	5.0430546		13.777896	102

Table 2

View Article Online
DOI: 10.1039/C9SE00259F

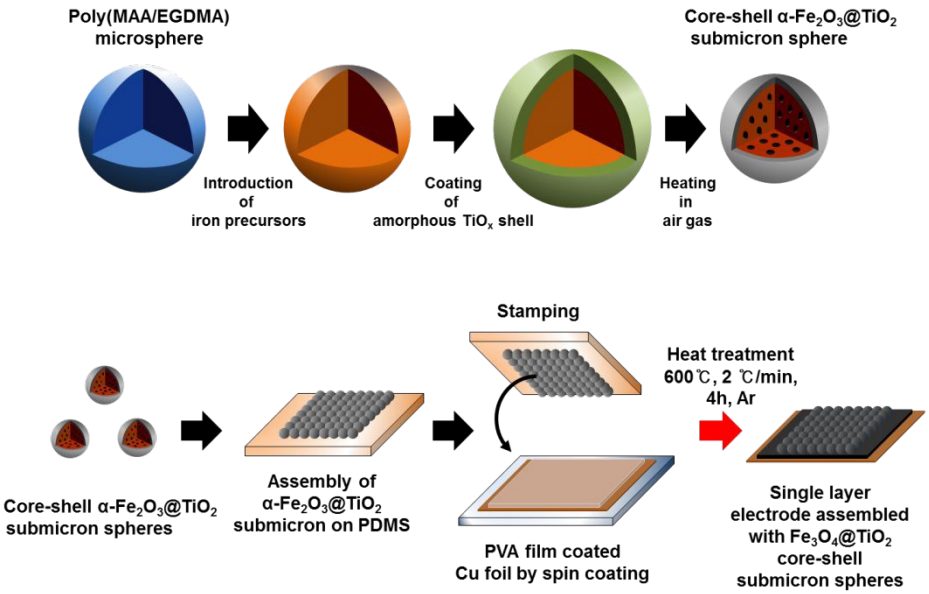

Figure 1

View Article Online
DOI: 10.1039/C9SE00259F

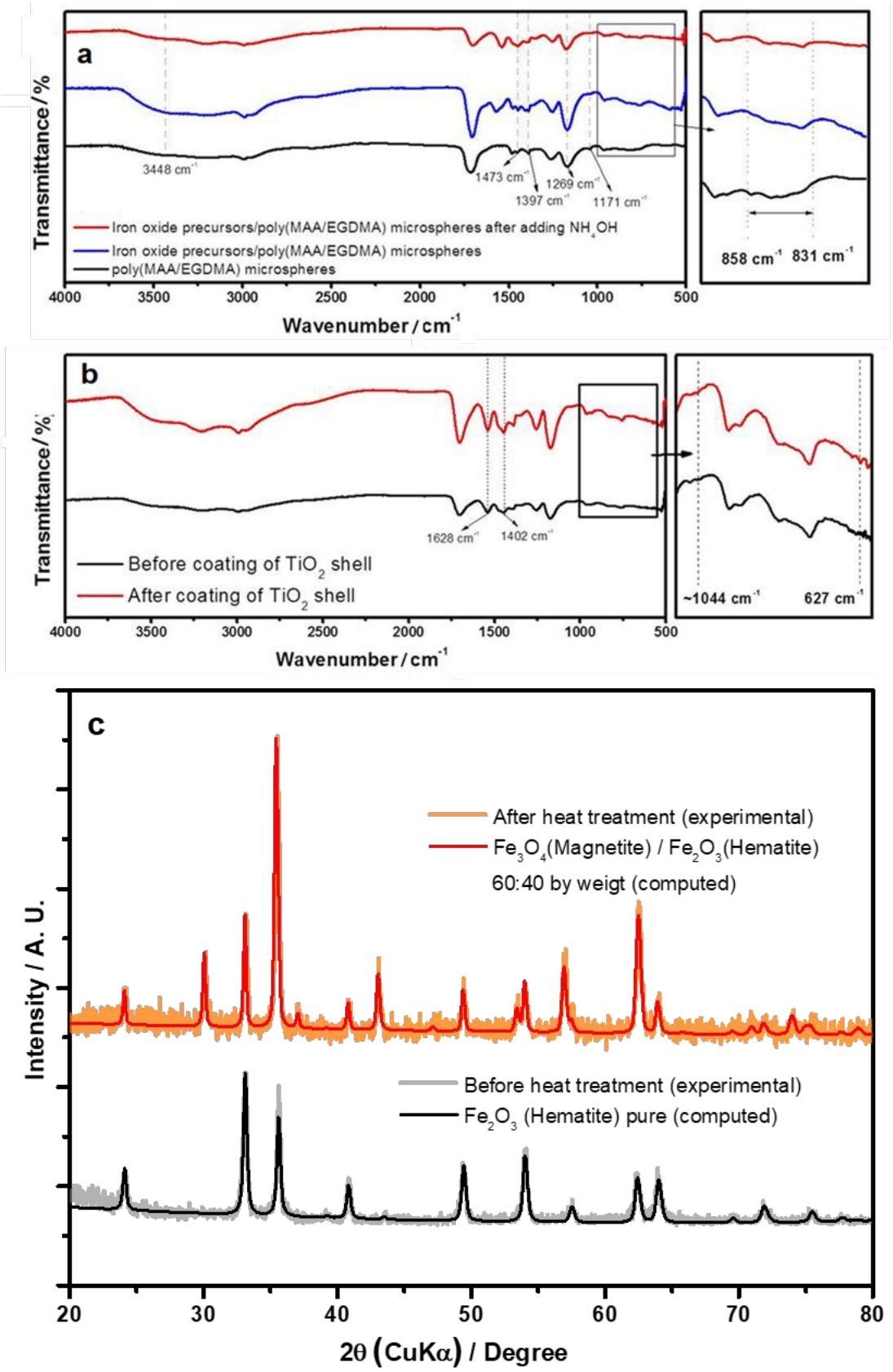

Figure 2

View Article Online
DOI: 10.1039/C9SE00259F

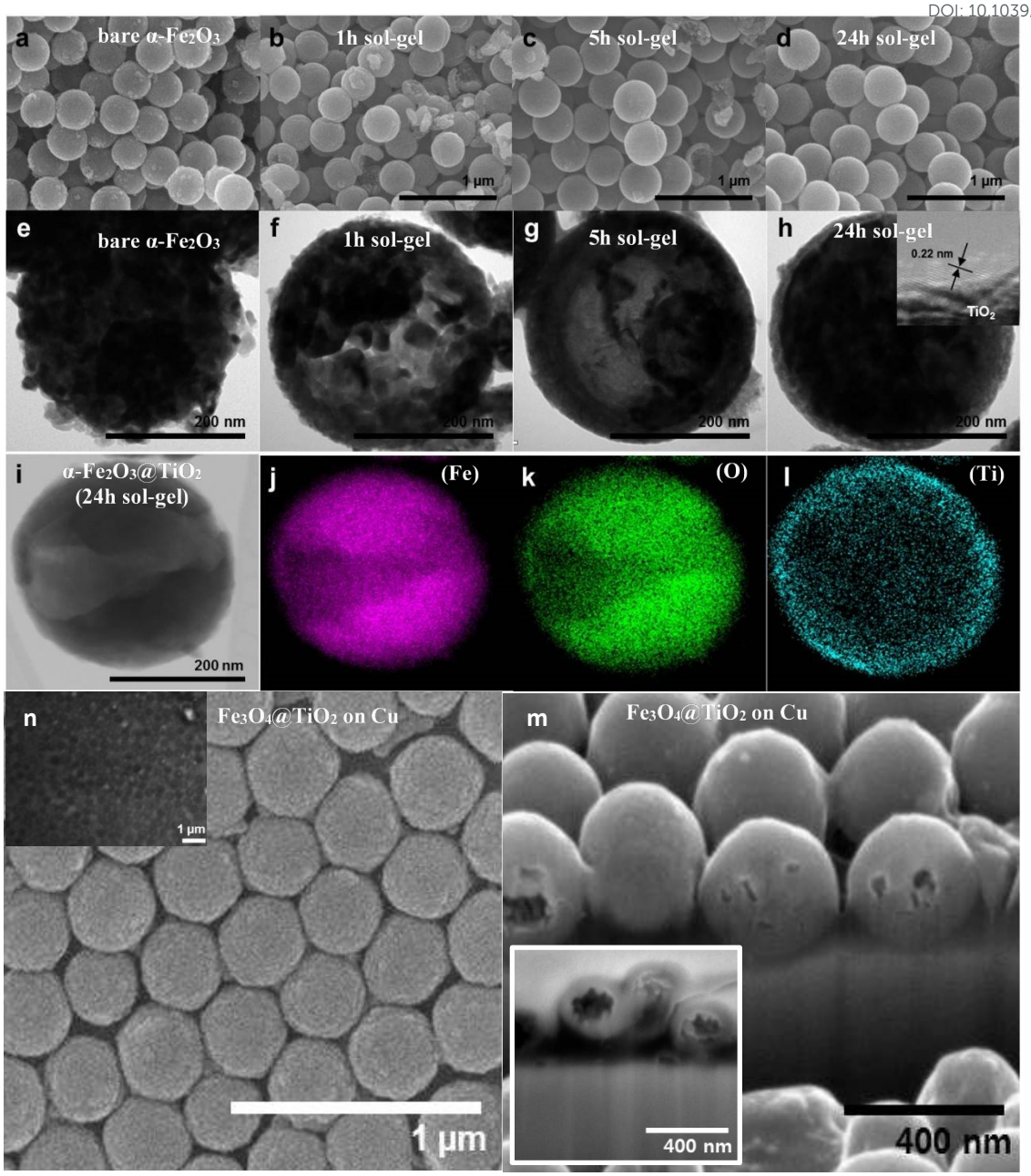

Figure 3

View Article Online
DOI: 10.1039/C9SE00259F

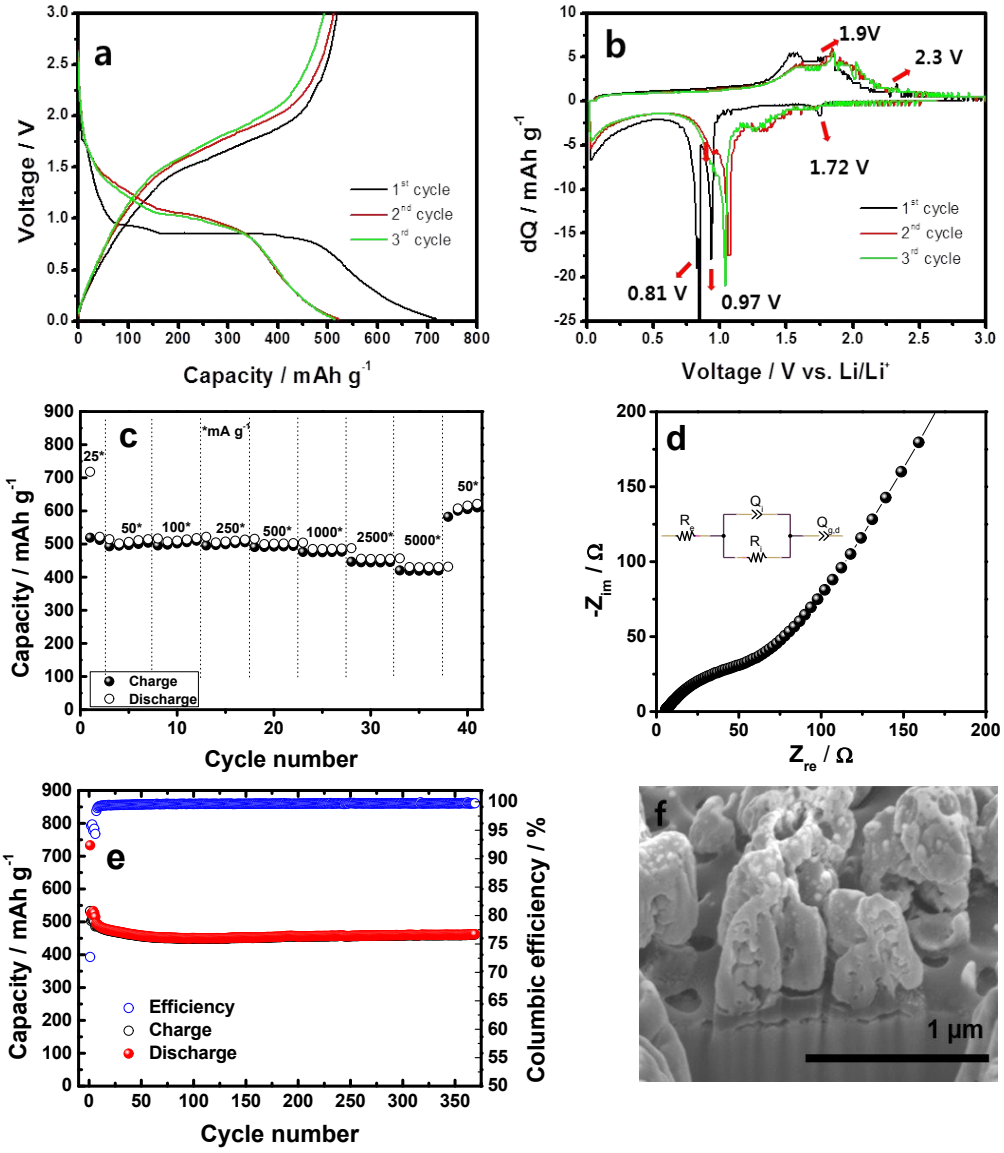

Figure 4

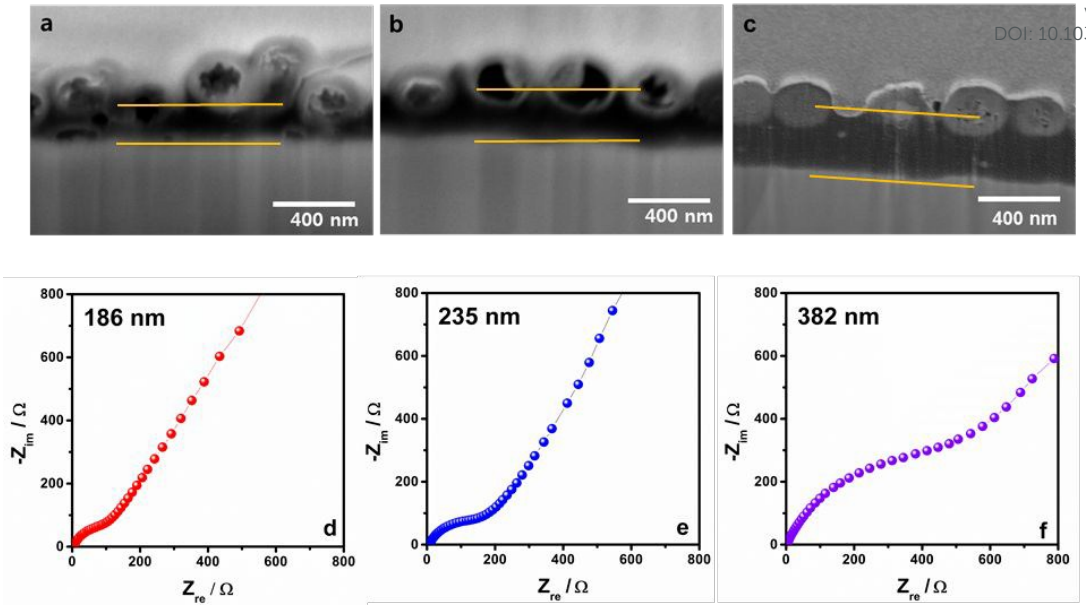

Figure 5

ToC figure

View Article Online
DOI: 10.1039/C9SE00259F